PCCP

PAPER

View Article Online
View Journal | View Issue

Cite this: *Phys. Chem. Chem. Phys.*, 2021, **23**, 23655

Low-dimensional HfS_2 as SO_2 adsorbent and gas sensor: effect of water and sulfur vacancies†

Amina Bouheddadj, [a] Tarik Ouahrani, *[a] Wilfried G. Kanhounnon, [b] Boufatah M. Reda, [a] Sumeya Bedrane, [c] Michael Badawi [d] and Ángel Morales-García *[e]

Received 4th September 2021,
Accepted 14th October 2021

DOI: 10.1039/d1cp04069c

rsc.li/pccp

First-principles based on density functional theory (DFT) calculations were performed to investigate the interaction of two-dimensional (2D) HfS_2 with SO_2, a harmful gas with implications for climate change. In particular, we describe the effect of water and sulfur vacancies on such interaction. The former promotes the physisorption of SO_2, whereas the latter promotes its chemisorption with structural changes on the absorbing surface. The results show that both structures are exothermic to adsorb the SO_2 molecules, but the adsorption type is different. The reaction of the stable structure in the presence of water with the sulfur oxides is a physisorption interaction that enhances the band gap value of the isolated monolayer. However, for the defective structure, we have a chemisorption interaction type, where the adsorption of SO_2 molecules widens the band gap values. To understand this behavior, we used Bader charge calculations and the noncovalent interactions index. While the water enhances the charge transfer between the monolayer and the adsorbed gas, the results show, however, that the defective structure is a more favorable gas sensor due to the metallic edge of the active site.

1 Introduction

The development generated during the Industrial Revolution has contributed notoriously to the emissions of greenhouse gases due to our dependency on fossil fuel combustion, petroleum refinement, and transport vehicles, to name a few.[1] Among such gases, sulfur oxides SO_x (SO_2 and SO_3) are air pollutants that alter the atmosphere of our planet,[2,3] and their mitigation is a challenge.[4–6] SO_x along with NO_x (*i.e.*, N_2O, NO and NO_2) contribute to damage to our environment by promoting acid rain, photochemical smog, and ozone layer destruction. In addition, such acid gases are also one of the major public health problems because of respiratory diseases.[7] The removal of these harmful gases has been the subject of many studies and a great challenge for innumerable experimental and theoretician groups.[8–13] In this context, wet flue gas desulfurization (FGD) and selective catalytic reduction (SCR) are the most broadly used technologies for SO_x abatement in industrial effluents and for NO_x removal from automotive exhaust gases to complement the three-way-catalyst system (TWC) in particular for diesel engines.[14–18]

Stringent environmental regulations have accelerated the development of low-cost, less energy-consuming strategies. One of them is SO_x capture and sequestration, inspired by the technology developed for CO_2 capture and sequestration (CCS).[19] The process is based on a gas sensor that captures SO_x from both static sources like industries and power plants and ambient air, followed by recycling for further utilization (as H_2SO_4 for example) or permanent sequestration in order to mitigate S_x emissions. From a physico-chemical point of view, the sensing mechanism is based on SO_x adsorption over suitable supports.[20–22] Furthermore, porous materials, activated carbon, and zeolites have been experimentally used as SO_x adsorbents.[23–28] In addition, recent investigations into two-dimensional (2D) systems have shown promising performance due to the intrinsic exposed large surface area and the affinity for SO_x such as graphene[29] and AlN monolayer.[30]

The understanding of the adsorption mechanism is of fundamental knowledge for manufacturing efficient sensors based on 2D materials. Indeed, the gas adsorption (SO_2 in our case) is the very first step before its reaction with the mechanism discussed below. 2D carbon-derived materials have

[a] *Laboratoire de Physique Théorique, Université de Tlemcen, 1300, Algeria. E-mail: tarik_ouahrani@yahoo.fr*
[b] *Laboratoire de Chimie Théorique et de Spectroscopie Moléculaire (LACTHESMO), Université dAbomey-Calavi, Benin*
[c] *Laboratory of Catalysis and Synthesis in Organic Chemistry, University of Tlemcen, Tlemcen, BP 119, Algeria*
[d] *Université de Lorraine and CNRS, LPCT, UMR 7019, 54506 Vandoeuvre-lés-Nancy, France*
[e] *Departamentde Cièncіade Materials i Química Física & Institutde Química Teórica i Computacional (IQTCUB) Universitatde Barcelona, c/Martíi Franquès 1-11, 08028, Barcelona, Spain. E-mail: angel.morales@ub.edu*

† Electronic supplementary information (ESI) available. See DOI: 10.1039/d1cp04069c

been proved as efficient substrates for oxygen-derived molecular compounds like SO_2, which is oxidized to SO_3.[25,31,32] Furthermore, it was found that the functionalization of these carbon-derived compounds with oxygen improves the reactivity towards SO_2.[33–35] These studies have contributed to understanding the interaction mechanism. However, they did not include the effect of water on the simulations. Thus, further realistic results are required by considering the presence of water, as it is always present in the ambient air together with SO_x. In fact, the presence of contaminants such as water drastically changes the adsorption performance and kinetics of zeolites in the case of CO_2 capture.[36,37]

Lizzio and DeBarr,[25] showed that the trapping ability of SO_2 molecules depends on the concentration of empty active sites and the grade of oxygenation on the surface. The study shows that the SO_2 adsorption capacity of activated char was found to be inversely proportional to the amount of oxygen adsorbed on its surface. Consequently, one way to adsorb SO_2 gas requires a desulfurization reaction. However, another way was developed to overcome the problem of reactivity between SO_2 and the surface, namely the use of naturally formed monatomic vacancy defects.[25] For instance, physical or chemical modifications like a change in the nature of the band structure of the graphene surface have been shown to boost its gas sensor performance.[38] Besides, S vacancy in MoS_2[39] or SnS_2[40] monolayers, showed stronger chemisorption and a noted change in their electronic properties, yielding better gas sensor and storage devices. Additionally, it has been demonstrated experimentally by the physical vapor method[41] that the single sulfur vacancy in MoS_2 leads to a stable structure with low formation energy, and the use of reduced MoS_2 to capture gas molecules such as O_2, NO, NH_3, CO_2, NO_2, and CH_4 is enhanced.[39,42]

Experimental studies by Mochida[43] and Lizzio[25] showed that adsorbed SO_2 at the surface of activated carbon is oxidized into adsorbed SO_3 by reaction with molecular oxygen in the vicinity of the active site or/and with an oxygen atom from the solid surface (C–O). The adsorbed SO_3 further reacts with a water molecule to form sulfuric acid H_2SO_4 while the free active site is restored. The production of H_2SO_4 proceeds indefinitely until saturation of the adsorbent, in which case, regeneration is required by water wash (liberating diluted sulfuric acid solution).

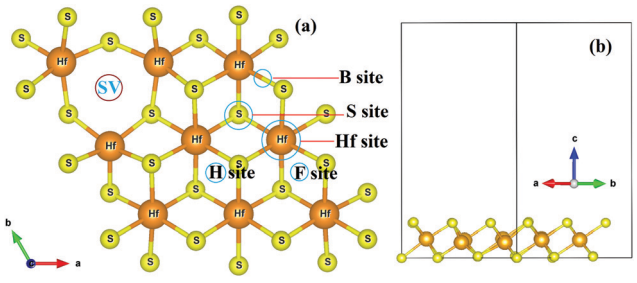

Fig. 1 (a) the top and (b) the side views of the most stable configuration of S v-2D-HfS_2 structure. The plot shows also the active sites and the S_v position on the studied monolayers. The bull in blue represent the oxygen atoms. Bridge (B), top on S atom (S), top on Hf atom (Hf), H and F positions represent the actives sites tested.

Thermal regeneration (>400 °C) is not suitable because it decomposes adsorbed H_2SO_4 into SO_2 and water. We expect a similar mechanism at the surface of the HfS_2 monolayer as its surface includes sulfur vacancies as active sites and surface oxygen atoms upon exchange with water molecules. Based on this, we investigated by density functional theory (DFT) and thermodynamic calculations the adsorption of SO_2 onto the HfS_2 monolayer to check its efficiency as a SO_x sensor. After describing our computational methods, we will first investigate the dynamic stability of the HfS_2 monolayer before evaluating its surface chemistry evolution under the presence of water. Then the adsorption of SO_2 will be assessed for realistic surfaces, including partially oxygenated and defective ones. The adsorption will be described with several tools, such as Bader[44] and NCI[45,46] analysis. Subsequent electronic properties will be determined. We will finally deliver the conclusions and perspective of this work.

2 Calculations settings

First-principles density-functional theory (DFT) based calculations were performed by using the Vienna *Ab initio* Simulation Package (VASP).[47,48] The ion-electron interactions were described using the projector augmented plane wave potential (PAW).[49] For the exchange–correlation functional, we employed the generalized gradient approximation (GGA), proposed by Perdew, Burke, and Ernzerhof (PBE).[50] Grimme's DFT-D3/BJ with Becke–Jonson damping[51, 52] dispersion correction approach was also considered to include the contribution of the London dispersion interactions. The planewave energy cutoff was set at 500 eV. The convergence criterion of the self-consistency process between successive iterations was set at 10^{-8} eV, and the Hellman–Feynman force on each relaxed atom was less than 0.03 eV $Å^{-1}$. The Brillouin zone was sampled by using a $7 \times 7 \times 1$ Γ-centered k-point grid within the Monkhorst–Pack scheme.[53] A large supercell $p(3 \times 3)$ of HfS_2 monolayer containing 27 atoms (9 Hf and 18 S atoms) was modeled within a 20 Å vacuum along the z-axis to avoid interactions between the adjacent molecules and slabs, see Fig. 1, respectively. Further analyses were performed with larger supercell models $p(4 \times 4)$ and $p(5 \times 5)$. Analogous electronic and adsorbing properties were found on the $p(3 \times 3)$ one. Therefore, the former $p(3 \times 3)$ supercell is sufficient to avoid the lateral interactions between adsorbed molecules. Furthermore, the hybrid Heyd–Scuseria–Ernzerhof functional (HSE06)[54] was employed to simulate accurately the band gap to avoid the underestimation of the GGA density functional.[55] Due to the presence of Hafnium atoms, the effect of spin–orbit was taken into account in the calculation of electronic properties by a second variational method.[56]

On the other hand, the dynamical stability of our monolayered HfS_2 was evaluated by the phonon dispersion as implemented in Phonopy.[57] Vibrational modes were calculated within the framework of finite displacement (FD) method.[58] This method allowed for the inclusion of van der Waals interactions in phonon/VASP calculations. Finally, the thermal

stability was also analyzed by performing molecular dynamics (MD) based-simulations. The MD was carried out using the NVT ensemble and controlled by the Nose–Hoover method[59–61] with a temperature set at 300 K for a total of 6 ps. The charge transfer induced by the interaction between the HfS_2 monolayer and the adsorbed gas molecules SO_2 was estimated using Bader charge analysis.[44] The adsorption energy on the surface was defined as: $E_{ads} = E_{(gas+HfS_2)} - E_{HfS_2} - nE_{gas}$. $E_{(gas+HfS_2)}$ represents the total energy of the optimized adsorption configuration. Meanwhile, E_{HfS_2} and E_{gas} stand for the energies of the calculated monolayer and target molecule, respectively, and n is the total number of molecules. According to such a definition, the more negative the adsorption, the more exothermic and favorable the interaction.

3 Results and discussions

3.1 Stability of the pristine HfS_2 mono-layer

We first analyzed in detail the stability of the 1T-HfS_2 structure by investigating its structural properties, stability (*i.e.*, mechanical, dynamical, and thermal) based on Born criteria, phonon spectra, and *ab initio* molecular dynamics (AIMD) simulations. The optimized lattice parameter was found to be equal to 3.64 Å, consistent with previous theoretical values of 3.61 Å[62] and 3.65 Å.[63] To investigate the dynamical stability of the pristine structure, the phonon dispersion curve was calculated. Fig. 2 shows the phonon dispersion plot along with the high symmetry points in the Brillouin Zone (BZ) of the trigonal system. We took care to plot two cases, one with VDW interactions including the LO/TO correction, and the second one without it. The figure shows that the inclusion of VDW correction terms leads to rising in most of the phonon frequencies due to increased atomic force constants brought by the additional energy terms. We point out that the absence of soft-phonon modes (*i.e.*, imaginary frequencies), indicates the dynamical stability of 1T-HfS_2. The irreducible representation is composed of nine vibrational modes, $\Gamma = A_{1g}(R) + E_g(R) + 2E_u(IR) + 2A_{2u}(IR)$, where IR and R notation indicate Infrared and Raman active modes, respectively, of which one A_{2u} and one E_u are acoustic modes. Note that they are incompatible due to the center inversion symmetry of the HfS_2 monolayer, see Fig. 2. Furthermore, due to the LO–TO correction, there is a split between the longitudinal (L) and transverse (T) optical phonon branches due to long-range Coulombic interactions that significantly affect the lattice dynamics at the Γ point. Such a trend ultimately depends on the symmetry of the crystal structure, which also determines the phonon transport in the crystal. We can also remark that the ZA branch in the phonon dispersion does not have a perfect parabolic form. This trend was discussed in relation to the bulk counterpart of HfS_2, see ref. 64. According to this study, the split results mainly from the polarizability of the system, and, from the hybridization between in-plane and out-of-plane atomic vibrations, which is an indication that the HfS_2 has nontrivial, and possibly anisotropic Born effective charge tensors.[64]

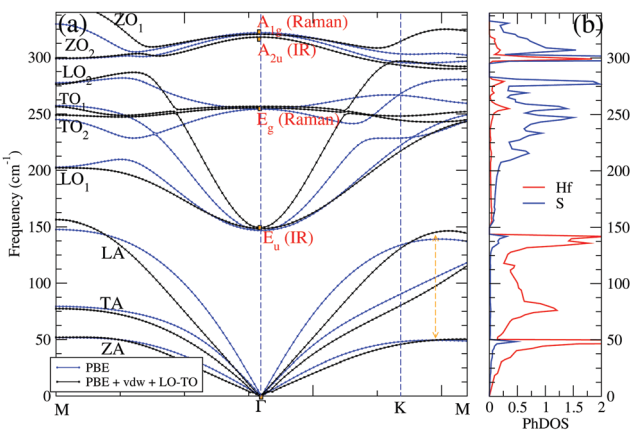

Fig. 2 Phonon dispersion curves and its corresponding phonon density of states (PhDOS) calculated using the PBE and PBE+vdw DFT models. The plot shows that nine phonon branches are defined by longitudinal acoustic (LA) and optical (LO), transverse acoustic (TA) and optical (TO), and out-of-plane acoustic (ZA) and optical (ZO) symbols. The blue curve stands for PBE calculation and the black one stands for the PBE+vdw + LO/TO correction.

Furthermore, the 2D optimized structure having a trigonal (1T) shape requires the calculation of two elastic constants (C_{11}, C_{12}). We found $C_{11} = 112.63$ N m^{-1} and $C_{12} = 25.59$ N m^{-1}, in good agreement with the reported ones of ref. 65, where $C_{11} = 141.98$ N m^{-1} and $C_{12} = 25.95$ N m^{-1}. These values satisfy the Born–Huang criteria for a 2D trigonal structure ($C_{11} > 0$ and $C_{11} - C_{12} > 0$),[66,67] indicating that the HfS_2 monolayer is mechanically stable. In addition, we can also deduce the shear modulus $G = 43.52$ (N m^{-1}), Young's modulus $C_{2D} = \frac{C_{11}C_{22} - C_{12}^2}{C_{11}} = 106.81$ (N m^{-1}). In addition, this value suggests that the HfS_2 monolayer has great resistance to unidirectional compression compared to shear deformation. These results are comparable to the synthetized MoS_2 (122 N m^{-1}).[68] However, the studied material is less rigid than graphene, whose C_{2D} is equal to 330 N m^{-1}. The thermal stability of the HfS_2 monolayer was also analyzed at ambient temperature within the MD simulation. The total energy oscillation and temperature at ambient and 600 K are gathered in Fig. 3. We note that no bond-breaking or structural distortion was observed during the MD simulation, even after 6 ps. In short, we assume that the synthesis of HfS_2 monolayer may be achievable at room temperature and even at high temperatures according to our detailed stability analysis.

3.2 Surface state in the presence of water

Once the stability of 1T-HfS_2 has been proved, we focus on the effect of water on the surface state of 1T-HfS_2 prior to the study of the adsorption of SO_2. We consider both adsorption of water and sulfur–oxygen atom exchanges, which can greatly modify the affinity of 1T-HfS_2 with SO_2. Thus, to get a more realistic view of the stability of the studied material, we report a 2D HfS_2 structure considering the sulfur and oxygen exchange and the H_2O adsorption simultaneously.

To search for the most stable geometry for H_2O molecules adsorbed, various configurations of water connected to different active sites on the surface of HfS_2 have been investigated, placing

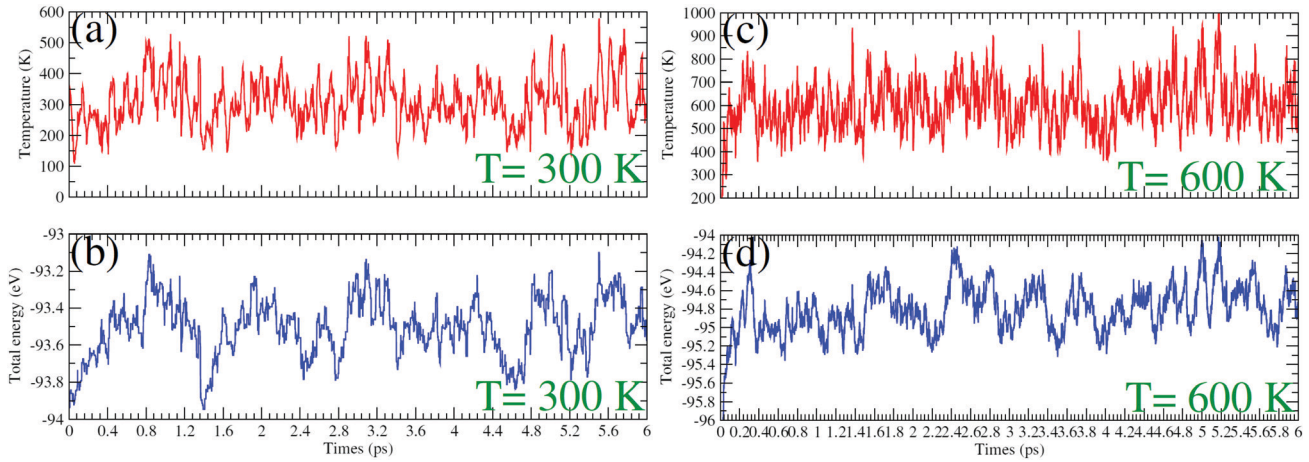

Fig. 3 MD simulation of temperature oscillations and energy fluctuations as a function of MD simulation time step at T = 300 and 600 K for the pure HfS_2 monolayer.

gas molecules at different adsorption sites with different orientations over the S and the top of Hf atoms. The favorable active sites are gathered in Table S1 and Fig. S1 of the ESI† and Fig. 1. No chemical bonds are formed and the only physisorption by means of weak interactions takes place on bare 1T-HfS_2. Negative adsorption energy was found for the more active site, namely that placed on the hafnium atoms, with a value of -23.7 kJ mol^{-1}. This indicates that the interaction between a water molecule and the basal plane of the sulfur surface is weak. This result is also comparable with what was found for MoS_2 monolayer where E_{ads} = -14.5 kJ mol^{-1} in ref. 69 or -13.5 kJ mol^{-1} in ref. 70, and even for graphene (E_{ads} = -11.6 kJ mol^{-1}).[69] This result is very comprehensible due to the very small affinity between oxygen and the sulfur atoms forming the surface of the investigated monolayer. The result is also more reasonable compared to what was already reported in ref. 63, where an unrealistic adsorption energy of -621.7 kJ mol^{-1} was reported.

The exchange reactions have been studied using water as the source of oxygen (see ESI†). Due to the fact we used a supercell $p(3 \times 3)$ in our calculations, the empirical formula including all atoms is Hf_9S_{18}. According to this, we can write the sulfur–oxygen (S/O) exchanges as follows:

$$Hf_9S_{18} + nH_2O = Hf_9S_{18-n}O_n + nH_2S \quad (1)$$

Because of the symmetry between the sides of 2D HfS_2, only one of the S layers was examined. Consequently, nine successive S/O exchanges were examined (n = 1 to 9) on the sulfur termination.

Table 1 shows the S/O exchange considering the progressive substitution of S atoms by O ones. The exchange is energetically favorable at a low concentration of O atoms. In particular, the first exchange is favorable by -23.2 kJ mol^{-1} (see Fig. S2 of the ESI†), but the second one is favorable by only -7.7 kJ mol^{-1}. From an exchange S/O ratio equal to 3 and above, the exchange is clearly unfavorable. Thus, this first analysis confirms that low partial pressure of water is demanded; otherwise, the 1T-HfS_2 could be passivated and, thus, inhibiting its sensibility towards SO_2. A step further consists of the inclusion of the temperature to obtain more realistic conditions at which 1T-HfS_2 could operate. The free enthalpies Δ_rG of the S/O exchange reactions were, therefore, determined according to the equation.[71–73]

Table 1 The calculated electronic contribution for the S/O exchange reaction from the reference surface ΔE_n. E_1 is the energy required to perform the nth exchange (kJ mol^{-1}), E_2 in the energy per exchanged oxygen atom $\Delta E_n/n$ (kJ mol^{-1})

n	E_1 (kJ mol^{-1})	ΔE_n (kJ mol^{-1})	E_2 (kJ mol^{-1})
1	−23.16	−23.16	−23.16
2	−7.72	−30.88	−15.44
3	9.65	−21.23	−7.04
4	54.03	32.81	8.20
5	32.81	65.61	13.12
6	52.10	117.71	19.59
7	50.17	167.88	23.93
8	70.43	238.32	32.99
9	93.59	331.91	36.86

$$\Delta_rG = \mu(Hf_9S_{18-n}O_n) - \mu(Hf_9S_{18}) + n\mu(H_2S) - n\mu(H_2O) \quad (2)$$

If we assume that the difference in the chemical potential of solid phases can be approximated by the difference in their electronic energy obtained by VASP, we obtain:[71–73]

$$\Delta_rG = \Delta E_n + \Delta\mu \quad (3)$$

ΔE_n corresponds to the electronic contributions calculated by eqn (1):

$$\Delta\mu = \Delta\mu^0(T) + R \times T \times \ln 10 \times \log\frac{P(H_2S)}{P(H_2O)} \quad (4)$$

is the difference between H_2S and H_2O chemical potentials.[71,74] The chemical potential ($\mu^0(T)$) includes the effect of temperature by accounting for the vibrational contribution of the system in the following equation:[71,72]

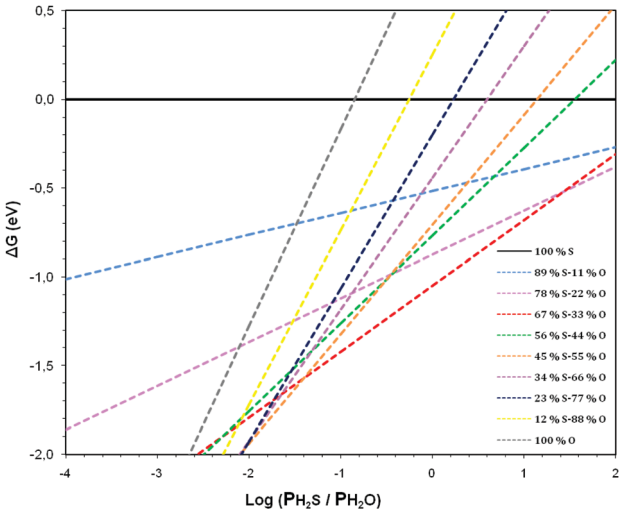

Fig. 4 Calculated diagram of variation of the Gibbs free energy ($\Delta_r G$) *versus* $\log\frac{P(H_2S)}{P(H_2O)}$ at T = 300 K.

$$\Delta\mu^0(T) = \Delta ZPE + \Delta H_{vib} + \Delta H_{rot} + \Delta H_{tr} - T(\Delta S_{vib} + \Delta S_{rot} + \Delta S_{tr}) \quad (5)$$

where ΔZPE, H, and S refer respectively to zero-point energy, enthalpy, and entropy for vibrational (vib), rotational (rot), and translational (tr) contributions.[75,76]

The stability of the different surfaces of the S/O exchange reactions was examined by plotting $\Delta_r G$ as a function of $\log\frac{(P(H_2S)}{(P(H_2O))}$, as shown in Fig. 4. The calculations were performed at T = 300 K and for a partial pressure ratio of 10^{-4} bar $< \frac{H_2S}{H_2O} < 10^2$ bar. Taking that the 100% sulfurized surface as the origin of $\Delta_r G$ = 0 eV highlighted by the black line in Fig. 4, we can stipulate that the most stable humid surface is obviously the one with three (O–S) exchanges, which corresponds to 33% of atoms of the surface of HfS_2 monolayer, for a partial pressure ratio in the range of 0.01 bar $< \frac{H_2S}{H_2O} <$ 0.10 bar.

We have also calculated E_{ads} for the oxygenated surface of HfS_2 monolayer ($HfS_{2-x}O_x$). We recall that the stable structure in the presence of water has 33% of its surface replaced by oxygen atoms. The presence of an oxygenated surface increases the affinity of additional water, reaching an adsorption energy of −80.61 kJ mol^{-1}. This stipulates that the 33% oxygenated surface captures more water fragments than the pure surface of the HfS_2 monolayer. Also, this trend shows that the pristine HfS_2 structure interacts very weakly with water. However, the adsorption can be approved if its surface is treated in the presence of water.

Finally, the effect of a single S-atom vacancy defect (Sv) is investigated on the adsorption of the H_2O molecule, see Fig. S3 of the ESI.† Thus, one sulfur atom is removed from the surface. Due to atomic relaxation, the structure is slightly deformed. Therefore, the bond lengths and angles nearest the vacancy atoms are changed, and this is depicted in Fig. S3 of the ESI.†

Table 2 Band gap (E_g) (eV) and calculated adsorption parameters: distance between the SO_2 and the surface (D) (Å), energy of adsorption (E_{ads}) (kJ mol^{-1}), the corrected energy of adsorption ($E_{adscorr}$ = E_{ads} + E_{ZPE}) in (kJ mol^{-1}). Here E_{ZPE} corresponds to zero-point energy (ZPE) of SO_2 molecule in the harmonic approximation and the charge transfer (Q_T)(electrons)

System	E_g	D	E_{ads}	$E_{adscorr}$	Q_T
Pure	2.12	4.43	−22.19	−3.86	−0.07
Sv-2D-HfS_2	2.29	2.06	−288.49	−270.16	−0.47
O-2D-HfS_2	2.51	2.19	−31.84	−13.51	−0.23

The results show that water may fill the vacancy site with an adsorption energy of −120.5 kJ mol^{-1}. Thus, in contrast to the pristine structure, the sulfur vacancy sites have a high affinity for water molecules due to the exposed metallic hafnium atoms. This energy is in agreement with the result found for a closed system by Qiang *et al.*[70] (−138.9 kJ mol^{-1}).

At this stage, let us calculate the adsorption energy of SO_2 molecules on the pristine (pure), oxygenated ($HfS_{2-x}O_x$), and Sv-defect (Sv-2D-HfS_2) structures. The values of adsorption energy E_{ads} of these three systems are listed in Table 2. Considering the pure structure, we have examined the adsorption of SO_2 on the same site used in ref. 77. We have found a value of E_{ads} = −22.2 kJ mol^{-1}, which is in a similar order to the results found by Chen *et al.*[77] of −26.1 kJ mol^{-1}. However, even with the weaker interactions found between SO_2 molecule and the pure HfS_2 monolayer, the physisorption is identified. Besides, we can also show in Table 2, and Fig. 5 that the adsorption of this molecule on oxygenated and Sv defect surfaces is more important than on pure ones. Obviously, the Sv-defect surface absorbs more strongly the SO_2 gas. Here, the energy of adsorption has a value of −288.5 kJ mol^{-1}. Whereas, the oxygenated structure (stable structure in the presence of water) of HfS_2 adsorbs the SO_2 gas with a value of −31.9 kJ mol^{-1} in the same order as the adsorption of this molecule by the pristine MoS_2 monolayer.[78] This means that this structure is more reactive and anchor stronger the SO_2 molecule. The result is similar to the one found for the $HfSe_2$ defect surface, which adsorbs the same molecule with a value of E_{ads} = −274.9 kJ mol^{-1}.[79]

The thermal correction was also calculated from the equation 2 and applied to correct the adsorption energy[80] for a temperature equal to 300 K. The result gives a value of −270.2 kJ mol^{-1}, showing the strong gas sensing in the Sv-2D-HfS_2 structure.

3.3 Influence of the SO_2 on electronic and bonding properties of the HfS_2 monolayer

To further understand the adsorption behaviors of SO_2 gas on the three investigated systems, the electronic properties of the HfS_2 monolayer with molecules adsorbed were calculated. However, it is mandatory to start by exploring the properties of the pristine 1T-HfS2 structure. The electronic band gap values were calculated at the PBE and HSE06 levels with and without spin–orbit coupling (SOC) correction and are represented in Table 3 and Fig. S4 of the ESI.† We note that the forthcoming analysis does not include this correction. This trend was already mentioned by Singh *et al.*[63] Additionally, as mentioned by these

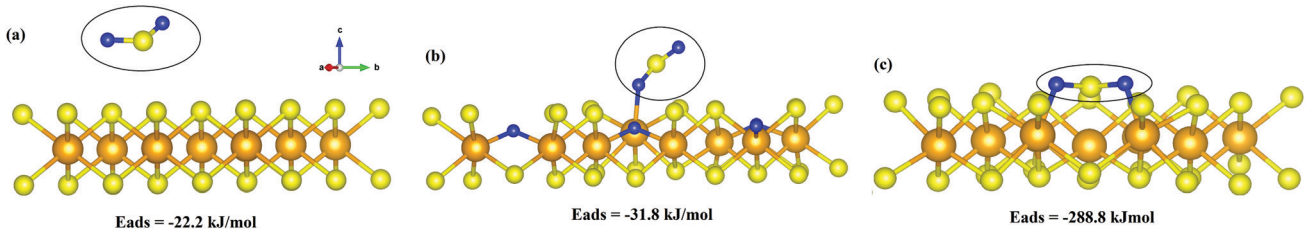

Fig. 5 Relaxed configurations of SO_2 adsorption on different surfaces: (a) pure (b) $HfS_{2-x}O_x$ and (c) Sv-2D-HfS_2. The SO_2 molecule is depicted with yellow and blue spheres which correspond to sulfur and oxygen atoms.

authors, we found that the 2D HfS_2 monolayer has a semiconducting nature with an indirect band gap with a value equal to 2.05 eV (see Fig. S3 of the ESI†), in fair agreement with the literature.[63,81,82] Interestingly, we note that the Sv structure has a metallic nature. This behavior was also shown in ref. 83. We also calculated the band gap values of 2D-HfS_2 pure, oxygenated ($HfS_{2-x}O_x$), adsorbed on pure structure (2D-HfS_2@SO_2), adsorbed on the oxygenated structure ($HfS_{2-x}O_x$@SO_2) and adsorbed on the Sv structure (Sv-2D-HfS_2@SO_2), see Table 3 and Fig. S5 of the ESI.† It is seen that while the SO_2 molecule is adsorbed on the oxygenated structure, we show a decrease in its band gap value. However, when the Sv-2D-HfS_2 adsorbs the SO_2, the band gap is widened. This trend is the opposite of what is shown in the case of the oxygenated surface. Finally, it is noted that there is no effect of the SO_2 molecule on the value of the band gap of the pure surface. It is also noted that the nature of the band gap becomes direct in the $HfS_{2-x}O_x$@SO_2 system, after the adsorption of the SO_2 gas.

The projected densities of states of pure and S v structures together with SO_2 are also calculated and gathered in Fig. S6 of the ESI.† It is worth mentioning that the vacancy defect (S v) structure does not keep its semiconducting behavior after the removal of one sulfur atom from its surface. In this case, the Hf-d orbital is localized on the E_F level,[83] yielding a metallic trend to the Sv structure. However, for the pure one, we show clearly that the Hf-d, S-p orbitals are the more dominant states near the Fermi level E_F. Additionally, we show a strong 3p-S/5d-Hf hybridization which governs this region. The projected density of states of the SO_2 shows that the S-s states dominate the region near the Fermi level (see Fig. S6 of the ESI†). This state will form lone pair-bonding in addition to a covalent one with the S v structure.

Before analyzing the effect of adsorption of SO_2 gas on the three investigated structures, we should recall that in all these cases, the SO_2 molecule was set at the top of the Hf atom. So, as expected, due to the strong adsorption energy, we show in Fig. 6(c), a new electronic level occurring near the Fermi level for Sv-2D-HfS_2@SO_2. In this case, the new state (S/O–p orbitals) originated from the SO_2 gas induces a hybridization with the 5d orbitals of Hf atoms near the S vacancy, creating a new Hf–O bonds through adsorption processes. This new bond eliminates the effect of defect states upon the adsorption of the SO_2 molecule. These findings are consistent with the creation of chemical O–Hf bonds clearly shown in Fig. 5(c). However, the effect of the SO_2 molecule on the pure structure is almost nil (see Fig. 6(a)). The plot does not exhibit notable PDOS of the adsorbed molecule on the surface of the monolayer. Also, in the $HfS_{2-x}O_x$@SO_2 case, the p–d hybridization shown in the S v case is also present, but with a weak effect (see Fig. 6(b)). Nevertheless, the interaction is mainly a physisorption type. The case where the adsorption energy is larger in the Sv case is due to the fact that the SO_2 molecule forms a chemisorption interaction with the surface of the Sv-2D-HfS_2 structure, which makes this structure a candidate for SO_2 gas sensor applications.

From above, it is demonstrated that the stable surface in the presence of water ($HfS_{2-x}O_x$), as well as the vacancy (Sv) ones, improves the sensing of SO_2 gas. Thus, it will be important to analyze the physisorption/chemisorption interaction between the SO_2 molecule and these surfaces. For this task, we will use the non-covalent interaction index (NCI). NCI can be investigated by identifying the low density of charge ρ and low reduced gradient s regions. Further, colored interactions can be classed conforming to their position on the $(\mathrm{sign}(\lambda_2)\rho(r))$ scale. $(\mathrm{sign}(\lambda_2))$ being the sign of the second eigenvalue of the Hessian matrix of ρ.[84,85] The domaines of blue color is referenced to strong attractive interactions $(\mathrm{sign}(\lambda_2)\rho(r) < 0)$, red regions for repulsive or closed-shell ones $(\mathrm{sign}(\lambda_2)\rho(r) > 0)$, and finally, the van der Waals $(\mathrm{sign}(\lambda_2)\rho(r) \simeq 0)$ domaines in the green color.

Table 3 The calculated band gap in (eV) of 2D-HfS_2 pure, vacancy defective (Sv-2D-HfS_2), oxygenated ($HfS_{2-x}O_x$), adsorbed on pure structure (2D-HfS_2@SO_2), adsorbed on oxygenated structure ($HfS_{2-x}O_x$@SO_2) and adsorbed on S v structure (Sv-2D-HfS_2@SO_2) at PBE, PBE + SOC, HSE06, and HSE06 + SOC levels. The results are compared to available theoretical data

	2D-HfS_2	S v-2D-HfS_2	$HfS_{2-x}O_x$	2D-HfS_2@SO_2	$HfS_{2-x}O_x$@SO_2	Sv-2D-HfS_2@SO_2
E_g(PBE)	**1.30**, 1.28[a]	0.00	1.98	1.31	1.62	1.44
E_g(PBE + SOC)	**1.22**	0.00	1.91	1.22	1.54	1.37
E_g(HSE06)	**2.13**, $\sim$ 2[b]	0.00	2.89	2.12	2.51	2.29
E_g(HSE06 + SOC)	**2.05**, (1.96, 2.13, 1.8, 1.87)[c]	0.00	2.82	2.03	2.44	2.22

[a] Ref. 63. [b] Ref. 81. [c] Experimental data quoted from ref. 82.

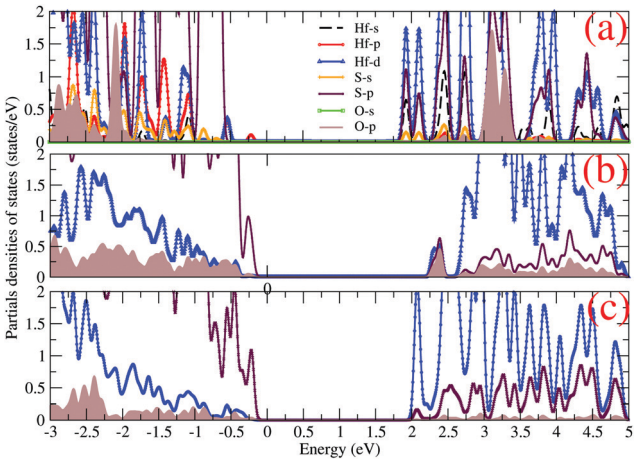

Fig. 6 Partial densities of states of (a) 2D-HfS_2@SO_2, (b)$HfS_{2-x}O_x$@SO_2 and (c) Sv-2D-HfS_2@SO_2 structures at the HSE06 level. Only the more important orbitals are highlighted in (b) and (c).

Fig. 7 and 8 show a large region with a green and orange disks isosurface. These ones are signs of the van der Waals interactions and repulsive ones governing both the Sv-2D-HfS_2@SO_2 and $HfS_{2-x}O_x$@SO_2 monolayers. The plots show an ionic interaction appearing in the form of hydrogen bonding between the hafnium and oxygen atoms (from SO_2 gas) in both Sv-2D-HfS_2@SO_2 and $HfS_{2-x}O_x$@SO_2 cases. These interactions are represented by blue spike isosurfaces. Dipole–dipole interactions, represented by a less blue isosurface, are also highlighted in these regions. Besides, no-bonded overlap colored in red is depicted between the sulfur of the HfS_2 surface and that of the SO_2 gas, see Fig. 7(a) and (b). Despite the resemblance of interaction types found in both investigated structures, some differences appear in the region where SO_2 is adsorbed. For example, the Steric repulsion is enhanced in the $HfS_{2-x}O_x$@SO_2 case, see Fig. 8(a) and (b). For this aim, a real chemisorption interaction is formed in the case S v-2D-HfS_2@SO_2 structure, while a physisorption interaction takes place in the $HfS_{2-x}O_x$@SO_2 system, with a strong hydrogen/dipole–dipole interaction bonding type. We also represented in Fig. S7(a) and (b) of the ESI,† the NCI plot of the case where the water molecule is adsorbed by both Sv-2D-HfS_2@HO_2 and $HfS_{2-x}O_x$@HO_2 systems, the interactions are identified as weak by the NCI index criteria due to the low density in the region of adsorption. However, Fig. S7(a) of the ESI† shows a much thicker bluish isosurface between Hf and H atoms of the H_2O molecule, indicating increased interaction strength due to the hydrogen bond and some deficit of electron density in the S vacancy site.

The charge density difference ($\Delta\rho$) between the SO_2 molecule and the investigated surfaces was also quantified using the quantum theory of atoms in molecules.[44,86] This quantity was calculated according to equation

$$\Delta\rho = \Delta\rho_{SO2+ML} - \Delta\rho_{ML} - \Delta\rho_{SO2}.$$

ρ_{SO2+ML}, ρ_{ML} and ρ_{SO2} are respectively, the total charge densities of the investigated monolayer with the adsorbed SO_2 molecule, the studied ML monolayer, and the SO_2 gas. The electron density difference plots are also gathered in Fig. 9(a) and (b). Herein, it is observed that the red and green isosurfaces indicate the gain and loss of electrons, respectively. The charge redistribution at the interface leads to strong electron accumulation between the SO_2 and the Sv-2D-HfS_2@SO_2 and $HfS_{2-x}O_x$@SO_2 systems.

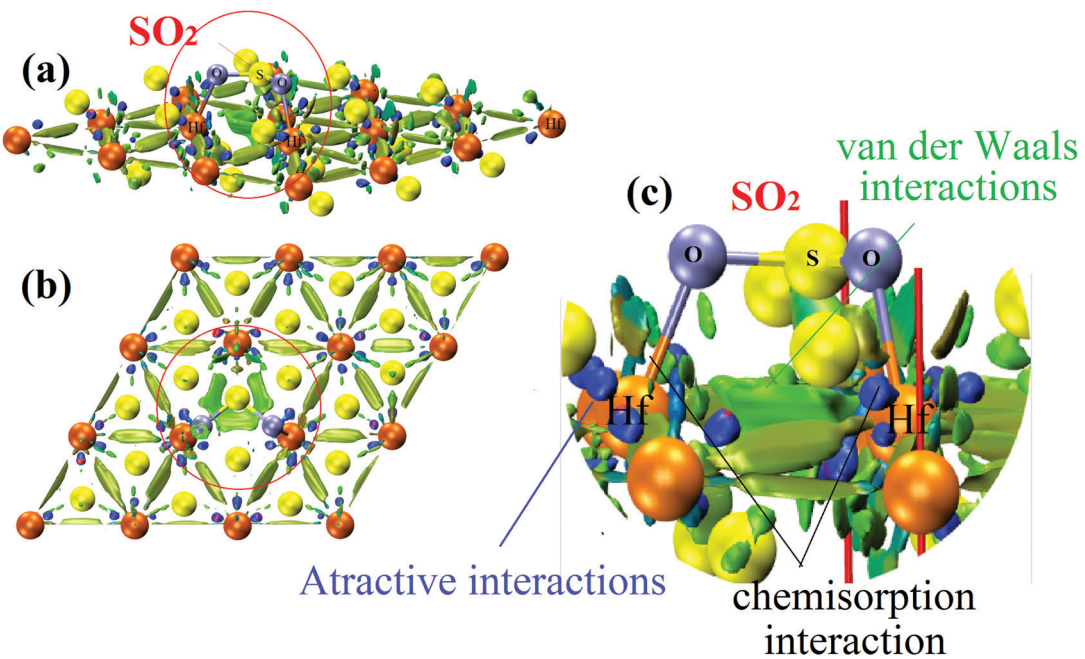

Fig. 7 (a) Side and (b) top views of NCI isosurfaces of the Sv-2D-HfS_2@SO_2 structure. Surfaces are colored in the [−0.04, 0.04] a.u. range of sign(λ_2)$\rho(r)$) (isovalue s = 0.23 a.u.). Repulsive interactions are shown as red isosurfaces, van der Waals interactions as thin, delocalized green regions, and strong attractive interactions as localized blue lentils. The plot in (c) represents a capture of the circled region.

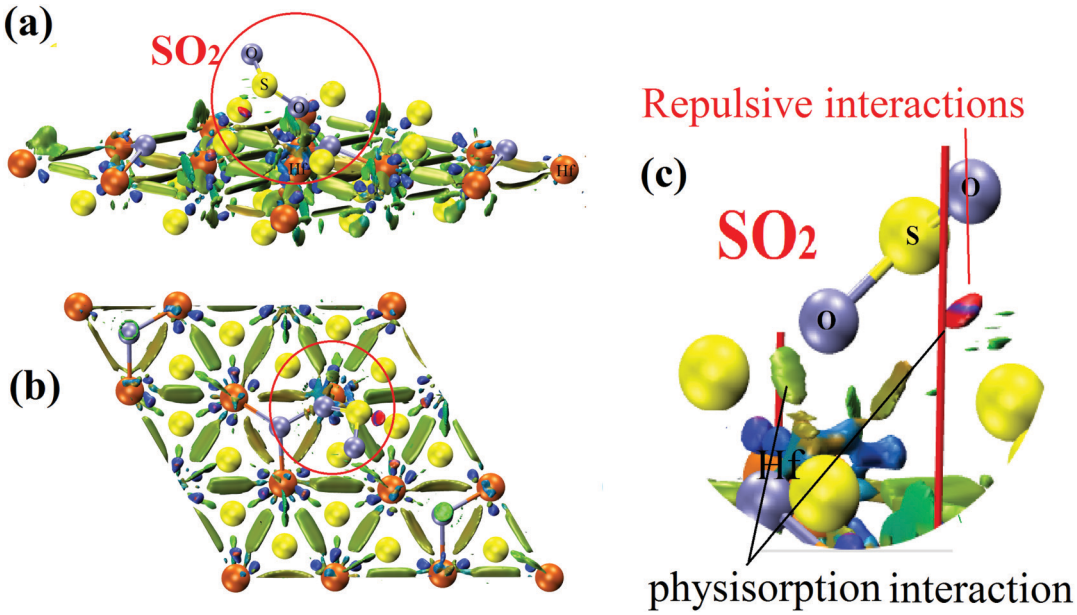

Fig. 8 (a) Side and (b) top views of NCI isosurfaces ($s(\mathbf{r})$ = 0.23 a.u.) of the $HfS_{2-x}O_x@SO_2$ structures. The plot in (c) represents a capture of the circled region.

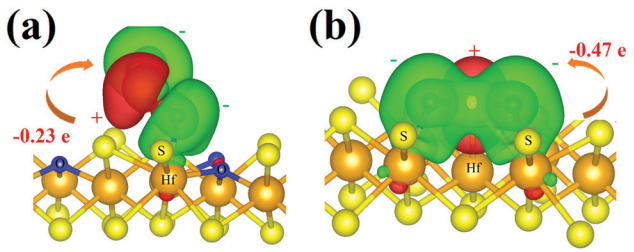

Fig. 9 The electron density difference plots of (a) $HfS_{2-x}O_x@SO_2$ (b) S *v*-2D-$HfS_2@SO_2$ structures.

Thus, the trend is enhanced around the O–Hf bond formed in the S*v* case. The calculation of charge transfer after the adsorption gives values of $Q_T = -0.47$ electrons and $Q_T = -0.23$ electrons for the S*v*-2D-$HfS_2@SO_2$ and $HfS_{2-x}O_x@SO_2$ systems respectively. Here, the charge transfer (Q_T) between the gas molecules and the monolayer is defined by $Q_T = Q_b - Q_a$, where Q_b and Q_a represent the net carried charge of gas molecules before and after adsorption. Notice that electron donation occurs through the bonds Hf–O. It is seen that the amount of charge transfer between SO_2 and the S*v*-2D-$HfS_2@SO_2$ surface is very comparable to a similar system with the $HfSe_2$ monolayer.[79] This study gives a value of $Q_T = -0.554$ electrons, whereas we have a charge transfer of the O atom to the surface of the S*v*-2D-$HfS_2@SO_2$ system of $Q_T = -0.47$ electrons. The small difference is mainly due to the difference in electron negativity between the Se and S atoms.

4 Conclusions

We show in this study that SO_2 gas can be adsorbed onto the HfS_2 monolayer in two different ways. The first one requires a stable structure in the presence of water, and the second is by removing one sulfur atom from its surface. To accomplish this task, we have employed a density functional theory procedure. Various adsorption sites and molecular orientations are involved in determining the most stable configuration. To investigate the effect of water on the surface state of the HfS_2 monolayer, we employed the strategy of exchanging a large number of basal sulfur atoms with oxygen atoms. We also show that the water treatment depends on the H_2S/H_2O pressure. The calculation of Gibbs energy at ambient temperature showed that the favored surface in the presence of water should contain 33% of oxygen atoms. By this, the adsorption energy with regard to water becomes four times more favorable than in the case of pure structure. The second way necessitates the use of a defect vacancy structure. This latter has significantly enhanced the adsorption of water. We calculated the values of adsorption energy of three cases: pure, defective, and stable in the presence of water. While the pure structure showed a very weak interaction with the SO_2 molecule, we noted that SO_2 uptake is lower. However, as the S vacancy structure offers a favored metallic active site, it makes the defective 2D-HfS_2 as SO_2 gas sensor more suitable.

Furthermore, we have analyzed the effect of SO_2 adsorption on both the electronic and bonding properties of the three involved structures. As expected, the electronic properties of the pristine structure due to the weak affinity between the adsorbed molecule and its surface remain untouched. The band gap value in a stable structure in the presence of water becomes larger. This trend is due to the enhancement of p–d hybridization between the adsorbed molecule and the processed surface. In the case of the defective structure, we note that S/O–p orbitals originated from the SO_2 gas induces a hybridization with the 5d orbitals of Hf atoms near the S vacancy, creating new Hf–O bonds through adsorption processes. In fact, the p orbital from the

adsorbed gas replaces the defective one, opening the band gap of the isolated defective structure. Based on topological Bader and NCI bonding analysis, we confirm the physisorption and chemisorption (with structural changes on the absorbed species) of SO_2 on HfS_2 in presence of water and defected HfS_2, respectively.

Data availability

All relevant data is available from the corresponding author upon reasonable request.

Author contributions

A. Bouheddadj, R. M. Boufatah and W. G. Kanhounnon: investigation, original draft. T. Ouahrani: supervision, project administration, conceptualization, formal analysis, writing – review & editing. Validation S. Bedrane: conceptualization, writing – review & editing M. Badawi writing – review & editing, resources. validation Á. Morales-García: writing – review & editing, conceptualization, formal analysis, validation.

Conflicts of interest

The authors declare that they have no known competing financial interests or personal relationships that could have appeared to influence the work reported in this paper.

Acknowledgements

The work is part of the PRFU project number B00L02-UN130120190004 registered at the University of Tlemcen. The work was also carried out at the University of Barcelona and has been supported by MCIN through grants RTI2018-09460-B-I00 and Juan de la Cierva (IJCI-2017-31979), and partly supported by the project PID2020-115293-RJ-I00 supported by MCIN/AEI/10.13039/501100011033. We would like to thank the PMMS (Pôle Messin de Modélisation et de Simulation) for providing us with the computational resources. T. O. is grateful to Prof. Alfonso Muñoz from Universidad de La Laguna for his help in the phonon dispersion calculations.

References

1 J. Clemens and C. Cuhls, Greenhouse gas emissions from mechanical and biological waste treatment of municipal waste, *Environ. Technol.*, 2003, **24**, 745–754, DOI: 10.1080/09593330309385611.

2 M. Nur, S. Sumariyah and A. Suseno, Removal of emission gas CO_x, NO_x and SO_x from automobile using non-thermal plasma, *IOP Conf. Ser.: Mater. Sci. Eng.*, 2019, **509**, 012085, DOI: 10.1088/1757-899X/509/1/012085.

3 R.-J. Huang, Y. Zhang, C. Bozzetti, K.-F. Ho, J.-J. Cao, Y. Han, K. R. Daellenbach, J. G. Slowik, S. M. Platt and F. Canonaco, High secondary aerosol contribution to particulate pollution during haze events in China, *Nature*, 2014, **514**, 218–222, DOI: 10.1038/nature13774.

4 G. Sugiyanto and S. Malkhamah, Model Pemilihan Moda Antara Mobil Pribadi dan Bis TransJogja Akibat Penerapan Biaya Kemacetan, *J. Transplant.*, 2009, **9**, 97–106, DOI: 10.26593/jtrans.v9i2.349.

5 H. Chu, T. W. Chien and S. Y. Li, Simultaneous absorption of SO_2 and NO from flue gas with $KMnO_4$/NaOH solutions, *Sci. Total Environ.*, 2001, **275**, 127–135, DOI: 10.1016/S0048-9697(00)00860-3.

6 V. Ramanathan and Y. Feng, Air pollution, greenhouse gases and climate change: Global and regional perspectives, *Atmos. Environ.*, 2009, **43**, 37–50, DOI: 10.1016/j.atmosenv.2008.09.063.

7 A. Rabl and J. V. Spadaro, Public health impact of air pollution and implications for the energy system, *Annu. Rev. Energy*, 2000, **25**, 601–627, DOI: 10.1146/annurev.energy.25.1.601.

8 Z.-H. Xu, X. Xiao, Y. Jia, P. Fang, J.-H. Huang, H.-W. Wu, Z.-J. Tang and D.-Y. Chen, Simultaneous Removal of SO_2 and NO by O_3 Oxidation Combined with Wet Absorption, *ACS Omega*, 2020, **5**, 5844–5853, DOI: 10.1021/acsomega.9b04031.

9 E. P. Hessou, W. G. Kanhounnon, D. Rocca, H. Monnier, C. Vallières, S. Lebègue and M. Badawi, Adsorption of NO, NO_2, CO, H_2O and CO_2 over isolated monovalent cations in faujasite zeolite: a periodic DFT investigation, *Theor. Chem. Acc.*, 2018, **137**, 1–12, DOI: 10.1007/s00214-018-2373-2.

10 A. A. Abdulrasheed, A. A. Jalil, S. Triwahyono, M. A. A. Zaini, Y. Gambo and M. Ibrahim, Surface modification of activated carbon for adsorption of SO_2 and NO_x: a review of existing and emerging technologies, *Renewable Sustainable Energy Rev.*, 2018, **94**, 1067–1085, DOI: 10.1016/j.rser.2018.07.011.

11 H. T. Zhao, T. Wu, J. He, S. Kingman, K. Q. Shi, D. Shen and Y. Y. Zhang, Simultaneous removal of SO_x and NO_x in flue gas at power stations over a Cu/Na-13X zeolite catalyst, *Adv. Mater. Res.*, 2013, **650**, 125–129, DOI: 10.4028/www.scientific.net/amr.650.125.

12 A. Nasonova and K.-S. Kim, Effects of TiO_2 coating on zeolite particles for NO and SO_2 removal by dielectric barrier discharge process, *Catal. Today*, 2013, **211**, 90–95, DOI: 10.1016/j.cattod.2013.03.006.

13 J.-H. Park, J.-W. Ahn, K.-H. Kim and Y.-S. Son, Historic and futuristic review of electron beam technology for the treatment of SO_2 and NO_x in flue gas., *Chem. Eng. J.*, 2019, **355**, 351–366, DOI: 10.1016/j.cej.2018.08.103.

14 F. Rezaei, A. A. Rownaghi, S. Monjezi, R. P. Lively and C. W. Jones, SO_x/NO_x Removal from Flue Gas Streams by Solid Adsorbents: A Review of Current Challenges and Future Directions, *Energy Fuels*, 2015, **29**, 5467–5486, DOI: 10.1021/acs.energyfuels.5b01286.

15 C. D. D. Giulio, J. A. Pihl, J. E. Parks, M. D. Amiridis and T. J. Toops, Passive-ammonia selective catalytic reduction (SCR): Understanding NH_3 formation over close-coupled three way catalysts (TWC), *Catal. Today*, 2014, **231**, 33, DOI: 10.1016/j.cattod.2014.01.027.

16 C. Tang, H. Zhang and L. Dong, Ceria-based catalysts for low-temperature selective catalytic reduction of NO with NH_3, *Catal. Sci. Technol.*, 2016, **6**, 1248–1264, DOI: 10.1039/C5CY01487E.

17 S. Bedrane, C. Descorme and D. Duprez, Investigation of the oxygen storage process on ceria-and ceria-zirconia-supported catalysts, *Catal. Today*, 2002, **75**, 401–405, DOI: 10.1016/S0920-5861(02)00089-5.
18 S. Bedrane, C. Descorme and D. Duprez, Oxygen storage and oxygen mobility on ceria and ceria-zirconia supported noble metalsStud, *Surf. Sci. Catal.*, 2001, **138**, 125–134, DOI: 10.1016/S0167-2991(01)80022-7.
19 A. Umar and Y.-B. Hahn, *Metal oxides nanostructures and their applications*, American Scientific Publishers, 2010, vol. 3.
20 C. Wang, L. Yin, L. Zhang, D. Xiang and R. Gao, Metal Oxide Gas Sensors: Sensitivity and Influencing Factors, *Sensors*, 2010, **10**(3), 2088–2106, DOI: 10.3390/s100302088.
21 S. Laribi, L. Dubois, G. De Weireld and D. Thomas, Simultaneous Absorption of SO_2 and CO_2 from Conventional and Partial Oxy-fuel Cement Plant Flue Gases, *Chem. Eng. Trans.*, 2018, **69**, 121–126, DOI: 10.3303/CET1869021.
22 I. Liemans, B. Alban, J. P. Tranier and D. Thomas, SO_x and NO_x absorption based removal into acidic conditions for the flue gas treatment in oxy-fuel combustion, *Energy Procedia*, 2011, **4**, 2847–2854, DOI: 10.1016/j.egypro.2011.02.190.
23 D. Lopez, R. Buitrago, A. Sepulveda-Escribano, F. Rodriguez-Reinoso and F. Mondragon, Low temperature catalytic adsorption of SO_2 on activated carbon, *J. Phys. Chem. C*, 2008, **112**, 15335–15340, DOI: 10.1021/jp802809c.
24 A. A. Lizzio and J. A. DeBarr, Effect of surface area and chemisorbed oxygen on the SO_2 adsorption capacity of activated char, *Fuel*, 1996, **75**, 1515–1522, DOI: 10.1016/0016-2361(96)00127-5.
25 A. A. Lizzio and J. A. DeBarr, Mechanism of SO_2 removal by carbon, *Energy Fuels*, 1997, **11**, 284–291, DOI: 10.1016/0016-2361(96)00127-5.
26 A. Srinivasan and M. W. Grutzeck, The adsorption of SO_2 by zeolites synthesized from fly ash, *Environ. Sci. Technol.*, 1999, **33**, 1464–1469, DOI: 10.1021/es9802091.
27 A. M. Shor and A. I. Rubaylo, IR spectroscopic study of SO_2 adsorption on modified Y zeolites, *J. Mol. Struct.*, 1997, **410-411**, 133, DOI: 10.1016/S0022-2860(96)09746-3.
28 I. C. Marcu and I. Sdulescu, Study of sulfur dioxide adsorption on Y zeolite, *J. Serb. Chem.*, 2004, **69**, 563–569, DOI: 10.2298/JSC0407563M.
29 H. Zhang, W. Cen, J. Liu, J. Guo, H. Yin and P. Ning, Adsorption and oxidation of SO_2 by graphene oxides: A van der Waals density functional theory study, *Appl. Surf. Sci.*, 2015, **324**, 61–67, DOI: 10.1016/j.apsusc.2014.10.087.
30 T. Ouyang, Z. Qian, X. Hao, R. Ahuja and X. Liu, Effect of defects on adsorption characteristics of AlN monolayer towards SO_2 and NO_2: *Ab initio* exposure, *Appl. Surf. Sci.*, 2018, **462**, 615–622, DOI: 10.1016/j.apsusc.2018.08.073.
31 A. B. Regina, J. Paulo, T. Zaragoza and P. G. David, Biomimetic Reactivity of Oxygen-Derived Manganese and Iron Porphyrinoid Complexes, *Chem. Rev.*, 2017, **117**(21), 13320–13352, DOI: 10.1021/acs.chemrev.7b00180.
32 R. Larciprete, S. Ulstrup, P. Lacovig, M. Dalmiglio, M. Bianchi, F. Mazzola, L. Hornekaer, F. Orlando, A. Baraldi, P. Hofmann and S. Lizzit, Oxygen Switching of the Epitaxial Graphene-Metal Interaction, *ACS Nano*, 2012, **6**, 9551–9558, DOI: 10.1021/nn302729j.
33 P. E. Fanning and M. A. Vannice, A DRIFTS study of the formation of surface groups on carbon by oxidation, *Carbon*, 1993, **31**, 721–730, DOI: 10.1016/0008-6223(93)90009-Y.
34 P. E. Fanning and M. A. Vannice, A DRIFTS study of Cu-ZSM-5 prior to and during its use for N_2O decomposition, *J. Catal.*, 2002, **207**, 166–182, DOI: 10.1006/jcat.2002.3518.
35 Y. Xiao, Q. Liu, Z. Liu, Z. Huang, Y. Guo and J. Yang, Roles of lattice oxygen in V_2O_5 and activated coke in SO_2 removal over coke-supported V_2O_5 catalysts, *Appl. Catal., B*, 2008, **82**, 114–119, DOI: 10.1016/j.apcatb.2008.01.004.
36 G. Li, P. Xiao, P. Webley, J. Zhang, R. Singh and M. Marshall, Capture of CO_2 from high humidity flue gas by vacuum swing adsorption with zeolite 13X, *Adsorption*, 2008, **14**, 415–422, DOI: 10.1007/s10450-007-9100-y.
37 Q. Al-Naddaf, S. Lawson, A. A. Rownaghi and F. Rezaei, Analysis of dynamic CO_2 capture over 13X zeolite monoliths in the presence of SO_x, NO_x and humidity, *AIChE J.*, 2020, **66**, e16297, DOI: 10.22541/au.158515657.77986013.
38 J. T. Robinson, F. K. Perkins, E. S. Snow, Z. Wei and P. E. Sheehan, Reduced graphene oxide molecular sensors, *Nano Lett.*, 2008, **8**, 3137–3140, DOI: 10.1021/nl8013007.
39 H. Li, M. Huang and G. Cao, Markedly different adsorption behaviors of gas molecules on defective monolayer MoS_2: A first-principles study, *Phys. Chem. Chem. Phys.*, 2016, **18**, 15110–15117, DOI: 10.1039/C6CP01362G.
40 R. Zhao, T. Wang, M. Zhao, C. Xia, X. Zhao, Y. An and X. Dai, A theoretical simulation of small-molecules sensing on an S-vacancy SnS_2 monolayer, *Phys. Chem. Chem. Phys.*, 2017, **19**, 10470–10480, DOI: 10.1039/C7CP00336F.
41 J. Hong, Z. Hu, M. Probert, K. Li, D. Lv, X. Yang, G. Lion, N. Mao, Q. Feng, L. Xie, J. Zhang, D. Wu, Z. Zhang, C. Jin, W. Ji, X. Zhang, J. Yuan and Z. Zhang, Exploring atomic defects in molybdenum disulphide monolayers, *Nat. Commun.*, 2015, **6**, 1–8, DOI: 10.1038/ncomms7293.
42 N. Yu, L. Wang, M. Li, X. Sun, T. Hou and Y. Li, Molybdenum disulfide as a highly efficient adsorbent for non-polar gases, *Phys. Chem. Chem. Phys.*, 2015, **17**, 11700–11704, DOI: 10.1039/C5CP00161G.
43 I. Mochida, Y. Korai, M. Shirahama, S. Kawano, T. Hada, Y. Seo, M. Yoshikawa and A. Yasutake, Removal of SO_x and NO_x over activated carbon fibers, *Carbon*, 2000, **38**, 227–239, DOI: 10.1016/S0008-6223(99)00179-7.
44 R. F. W. Bader, *Atoms in molecules: A quantum theory*, Clarendon Press, Oxford, UK, 1990, p. 438.
45 A. Otero-De-La-Roza and E. R. Johnson, A benchmark for non-covalent interactions in solids, *J. Chem. Phys.*, 2012, **137**, 054103, DOI: 10.1063/1.4738961.
46 H. Z. Guedda, T. Ouahrani, A. Morales-García, R. Franco, M. A. Salvadó, P. Pertierra and J. M. Recio, Computer simulations of 3C-SiC under hydrostatic and non-hydrostatic stresses, *Phys. Chem. Chem. Phys.*, 2016, **18**, 8132–8139, DOI: 10.1039/C6CP00081A.
47 G. Kresse and J. Furthmüller, Efficiency of ab-initio total energy calculations for metals and semiconductors using a

plane-wave basis set, *Comput. Mater. Sci.*, 1996, **6**, 15–50, DOI: 10.1016/0927-0256(96)00008-0.

48 G. Kresse and J. Hafner, Ab initio molecular dynamics for liquid metals, *Phys. Rev. B: Condens. Matter Mater. Phys.*, 1993, **47**, 558–561, DOI: 10.1103/PhysRevB.47.558.

49 G. Kresse and D. Joubert, From ultrasoft pseudopotentials to the projector augmented-wave method, *Phys. Rev. B: Condens. Matter Mater. Phys.*, 1999, **59**, 1758–1775, DOI: 10.1103/PhysRevB.59.1758.

50 J. P. Perdew, K. Burke and M. Ernzerhof, Generalized gradient approximation made simple, *Phys. Rev. Lett.*, 1996, **77**, 3865–3868, DOI: 10.1103/physrevlett.77.3865.

51 S. Grimme, J. Antony, S. Ehrlich and H. Krieg, A consistent and accurate ab initio parametrization of density functional dispersion correction (DFT-D) for the 94 elements H-Pu, *J. Chem. Phys.*, 2010, **132**, 154104, DOI: 10.1063/1.3382344.

52 S. Grimme, S. Ehrlich and L. Goerigk, Effect of the damping function in dispersion corrected density functional theory, *J. Comput. Chem.*, 2011, **32**, 1456–1465, DOI: 10.1002/jcc.21759.

53 H. J. Monkhorst and J. D. Pack, Special points for Brillouin-zone integrations, *Phys. Rev. B: Solid State*, 1976, **13**, 5188–5192, DOI: 10.1103/PhysRevB.13.5188.

54 J. Heyd, G. E. Scuseria and M. Ernzerhof, Hybrid functionals based on a screened Coulomb potential, *J. Chem. Phys.*, 2003, **118**, 8207–8215, DOI: 10.1063/1.1564060.

55 Á. Morales-García, R. Valero and F. Illas, An empirical, yet practical way to predict the band gap in solids by using density functional band structure calculations, *J. Phys. Chem. C*, 2017, **121**, 18862–18866, DOI: 10.1021/acs.jpcc.7b07421.

56 X. Ma, X. Wu, H. Wang and Y. Wang, A Janus MoSSe monolayer: a potential wide solar-spectrum water-splitting photocatalyst with a low carrier recombination rate, *J. Mater. Chem. A*, 2018, **6**, 2295–2301, DOI: 10.1039/C7TA10015A.

57 A. Togo and I. Tanaka, First principles phonon calculations in materials science, *Scr. Mater.*, 2015, **108**, 1–5, DOI: 10.1016/j.scriptamat.2015.07.021.

58 X. Gonze and C. Lee, Dynamical matrices, Born effective charges, dielectric permittivity tensors, and interatomic force constants from density-functional perturbation theory, *Phys. Rev. B: Condens. Matter Mater. Phys.*, 1997, **55**, 10355, DOI: 10.1103/PhysRevB.55.10355.

59 G. J. Martyna, M. L. Klein and M. Tuckerman, Nose-Hoover chains: The canonical ensemble via continuous dynamics, *J. Chem. Phys.*, 1992, **97**, 2635–2643, DOI: 10.1063/1.463940.

60 S. Nose, A Molecular Dynamics Method for Simulations in the Canonical, Ensemble, *Mol. Phys.*, 1984, **52**, 255–268, DOI: 10.1080/00268978400101201.

61 S. Nose, A Unified Formulation of the Constant Temperature Molecular Dynamics Methods, *J. Chem. Phys.*, 1984, **81**, 511–519, DOI: 10.1063/1.447334.

62 B. Wang, X. Luo, J. Chang, X. Chen, H. Yuan and H. Chen, Efficient charge separation and visible-light response in bilayer HfS_2-based van der Waals heterostructures, *RSC Adv.*, 2018, **8**, 18889–18895, DOI: 10.1039/c8ra03047b.

63 D. Singh, S. K. Gupta, Y. Sonvane, A. Kumar and R. Ahuja, 2D-HfS_2 as an efficient photocatalyst for water splitting, *Catal. Sci. Technol.*, 2016, **6**, 6605–6614, DOI: 10.1039/c6cy01172a.

64 J. Peng, S. Najmaei, M. Dubey and P. W. Chung, Dominant ZA phonons and thermal carriers in HfS_2, *J. Appl. Phys.*, 2019, **126**, 164302, DOI: 10.1063/1.5110515.

65 Q. Zhao, Y. Guo, K. Si, Z. Ren, J. Bai and X. Xu, Elastic, electronic, and dielectric properties of bulk and monolayer ZrS_2, $ZrSe_2$, HfS_2, $HfSe_2$ from van der Waals density-functional theory, *Phys. Status Solidi B*, 2017, **254**, 1700033, DOI: 10.1002/pssb.201700033.

66 M. Born and H. Huang, *Dynamical Theory of Crystal Lattices*, Clarendon, Oxford, 1954.

67 F. Mouhat and F. X. Coudert, Necessary and sufficient elastic stability conditions in various crystal systems, *Phys. Rev. B: Condens. Matter Mater. Phys.*, 2014, **90**, 224104, DOI: 10.1103/PhysRevB.90.224104.

68 X. Yang, D. Singh, Z. Xu, Z. Wang and R. Ahuja, An emerging Janus MoSeTe material for potential applications in optoelectronic devices, *J. Mater. Chem. C*, 2019, **7**, 12312–12320, DOI: 10.1039/c9tc03936h.

69 G. Levita, P. Restuccia and M. C. Righi, Graphene and MoS_2 interacting with water: A comparison by ab initio calculations, *Carbon*, 2016, **107**, 878–884, DOI: 10.1016/j.carbon.2016.06.072.

70 Q. Li, L. Shi, R. Wu, C. Lin, X. Bai, Y. Ouyang, B. A. K. P. Baraiya and J. Wang, Unveiling chemical reactivity and oxidation of 1T-phased group VI disulfides, *Phys. Chem. Chem. Phys.*, 2019, **21**, 17010–17017, DOI: 10.1039/C9CP02985K.

71 M. Badawi, S. Cristol, J. F. Paul and E. Payen, DFT study of furan adsorption over stable molybdenum sulfide catalyst under HDO conditions, *C. R. Chim.*, 2009, **12**, 754–761, DOI: 10.1016/j.crci.2008.10.023.

72 M. Badawi, J. F. Paul, S. Cristol, E. Payen, Y. Romero, F. Richard, S. Brunet, D. Lambert, X. Portier, A. Popov, E. Kondratieva, J. M. Goupil, J. El Fallah, J. P. Gilson, L. Mariey, A. Travert and F. Maugée, Effect of water on the stability of Mo and CoMo hydrodeoxygenation catalysts: A combined experimental and DFT study, *J. Catal.*, 2011, **282**, 155–164, DOI: 10.1016/j.jcat.2011.06.006.

73 J. W. Hounfodji, W. G. Kanhounnon, G. Kpotin, G. S. Atohoun, J. Lainé, Y. Foucaud and M. Badawi, Molecular insights on the adsorption of some pharmaceutical residues from wastewater on kaolinite surfaces, *Chem. Eng. Sci.*, 2021, **407**, 127176, DOI: 10.1016/j.cej.2020.127176.

74 D. Loffreda, Theoretical insight of adsorption thermodynamics of multifunctional molecules on metal surfaces, *Surf. Sci.*, 2006, **600**, 2103–2112, DOI: 10.1016/j.susc.2006.02.045.

75 P. W. Atkins, *Physical Chemistry*, Oxford University Press, London, 5th edn, 1990.

76 F. Jensen, *Introduction to Computational Chemistry*, John Wiley and Sons Ltd, 2nd edn, 2007, p. 433.

77 D. Chen, X. Zhang, J. Tang, Y. Li, Z. Cui and Q. Zhou, Using single-layer HfS_2 as prospective sensing device toward

typical partial discharge gas in SF_6-based gas-insulated switchgear, *IEEE Trans. Electron Devices*, 2018, **66**, 689–695, DOI: 10.1109/TED.2018.2882236.

78 A. Abbasi and J. J. Sardroodi, Adsorption of O_3, SO_2 and SO_3 gas molecules on MoS_2 monolayers: a computational investigation, *Appl. Surf. Sci.*, 2019, **469**, 781–791, DOI: 10.1016/j.apsusc.2018.11.039.

79 G. Yang, P. Yan, C. Zhu, Y. Gu, N. Lu, J. Xue, X. Zhang, R. Sun and X. Fang, Selenium Vacancy-Enhanced Gas Adsorption of Monolayer Hafnium Diselenide ($HfSe_2$) from a Theoretical Perspective, *Adv. Theory Simul.*, 2019, **2**, 1900052, DOI: 10.1002/adts.201900052.

80 Á. Morales-García, A. Fernández-Fernández, F. Vines and F. Illas, CO_2 abatement using two-dimensional MXene carbides, *J. Mater. Chem. A*, 2018, **6**, 3381–3385, DOI: 10.1039/C7TA11379J.

81 J. Kang, H. Sahin and F. M. Peeters, Mechanical properties of monolayer sulphides: a comparative study between MoS_2, HfS_2 and TiS_3, *Phys. Chem. Chem. Phys.*, 2015, **17**, 27742–27749, DOI: 10.1039/C5CP04576B.

82 H. Jiang, Structural and electronic properties of ZrX_2 and HfX_2 (X= S and Se) from first principles calculations, *J. Chem. Phys.*, 2011, **134**, 204705, DOI: 10.1063/1.3594205.

83 D. Singh and R. Ahuja, Enhanced opto-electronic and thermoelectric properties by intrinsic structural defects in monolayer HfS_2, *ACS Appl. Energy Mater.*, 2019, **2**, 6891–6903, DOI: 10.1021/acsaem.9b01402.

84 R. A. Boto, J. P. Piquemal and J. Contreras-García, Revealing strong interactions with the reduced density gradient: a benchmark for covalent, ionic and charge-shift bonds, *Theor. Chem. Acc.*, 2017, **136**, 139, DOI: 10.1007/s00214-017-2169-9.

85 S. Belarouci, T. Ouahrani, N. Benabdallah, A. Morales-García and I. Belabbas, Two-dimensional silicon carbide structure under uniaxial strains, electronic and bonding analysis, *Comput. Mater. Sci.*, 2018, **151**, 288–295, DOI: 10.1016/j.commatsci.2018.05.020.

86 T. Ouahrani, I. Merad-Boudia, H. Baltache, R. Khenata and Z. Bentalha, Effect of pressure on the global and local properties of cubic perovskite crystals, *Phys. Scr.*, 2011, **84**, 025704, DOI: 10.1088/0031-8949/84/02/025704.

